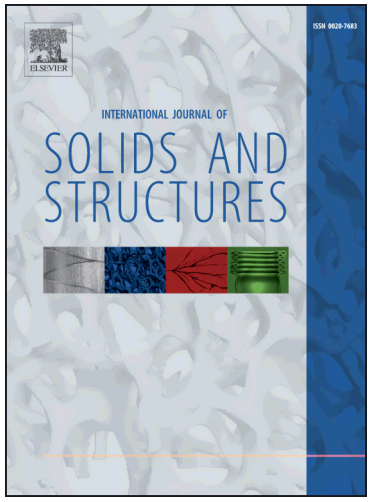

Study of localization in a void-sheet under stress states near pure shear

Viggo Tvergaard

PII: S0020-7683(15)00355-8
DOI: http://dx.doi.org/10.1016/j.ijsolstr.2015.08.008
Reference: SAS 8872

To appear in: *International Journal of Solids and Structures*

Received Date: 20 June 2015
Revised Date: 7 August 2015

Please cite this article as: Tvergaard, V., Study of localization in a void-sheet under stress states near pure shear, *International Journal of Solids and Structures* (2015), doi: http://dx.doi.org/10.1016/j.ijsolstr.2015.08.008

STUDY OF LOCALIZATION IN A VOID-SHEET UNDER STRESS STATES NEAR PURE SHEAR

Viggo Tvergaard
Department of Mechanical Engineering, Solid Mechanics
Technical University of Denmark, DK-2800 Kgs. Lyngby, Denmark
viggo@mek.dtu.dk

ABSTRACT – A recent study of a porous ductile material under pure shear has indicated that no failure is predicted, whereas a number of micro-mechanical analyses for simple shear have shown that a maximum shear stress is reached and failure occurs. Both simple shear and pure shear are characterized by zero stress triaxiality and in both types of stress states the analyses show that the voids collapse to micro-cracks. The possibility of failure in pure shear is further investigated here by studying the effect of an initial imperfection in the form of a row of circular cylindrical voids inclined to the principal tensile stress. A number of previous investigations have shown that such imperfections can lead to plastic flow localization in a shear band and subsequently lead to void- sheet fracture inside the band. The present analyses confirm that the imperfection results in localization failure, even at moderate or rather low stress triaxiality. But in pure shear, with zero stress triaxiality, no failure is predicted. Initially the imperfection results in increasing shearing along the row of voids, but this tendency towards increasing shearing is interrupted if the voids collapse to micro-cracks. For the largest imperfection considered, i.e. a relatively large ratio of the void radius to void spacing, there is still a range of stress states in the vicinity of pure shear, where no localization is predicted, and for smaller imperfections this range is larger.

KEYWORDS: Voids, low stress triaxiality, large strain plasticity, contact, pure shear.

1. INTRODUCTION

In ductile metals fracture typically occurs by the nucleation of voids that subsequently grow to coalescence. Sometimes, when shear localization takes place before final failure, voids grow to coalescence while they are being smeared out in what is called void-sheet failure. Such void-sheet failure was early observed in experiments (Rogers, 1960). In early applications of the Gurson model it was found that shear localization is predicted (Yamamoto, 1978; Tvergaard, 1981; Saje et al., 1982) resulting in subsequent void-sheet failure, both in cases where the bands initiate at a bifurcation from a homogeneous stress state and in cases where they grow from an imperfection. For a metal with two populations of voids the Gurson model has been used (Tvergaard, 1982) to show the failure mechanism, where localization occurs between two larger voids, leading to local void-sheet failure between the larger voids. There has also been numerical studies for a single layer of voids in a ductile solid (Tvergaard, 1989; Barsoum and Faleskog, 2011; Tekoglu et al., 2014), which directly show that this imperfection can result in void-sheet failure. Many research articles on ductile fracture

predictions have been summarized in a number of reviews (Garrison and Moody, 1987; Tvergaard, 1990; Benzerga and Leblond, 2010).

Recently there has been increasing interest in the behaviour of voids under low stress triaxiality. Barsoum and Faleskog (2007a) have carried out full 3D analyses for shear specimens containing spherical voids in order to model their experiments (Barsoum and Faleskog, 2007b) on ductile fracture in a double notched tube specimen loaded in combined tension and torsion. In a number of plane strain cell model analyses for a material containing a periodic array of circular cylindrical voids Tvergaard (2008, 2009, 2012), Dahl *et al.* (2012) and Nielsen *et al.* (2012) have shown that in stress states similar to simple shear the voids are flattened out to micro-cracks, which rotate and elongate until interaction with neighbouring micro-cracks gives coalescence. When the micro-cracks form, it is important to account for the contact between crack surfaces, where large contact stresses develop.

In recent experimental investigations for ductile fracture in shear, Bao and Wierzbicki (2004), Beese *et al.* (2010) and Dunand and Mohr (2011) have used special butterfly specimens to study the effect of the stress triaxiality and of the Lode angle, for two different aluminium alloys and a TRIP steel. Haltom *et al.* (2013) have used a tubular specimen in tension-torsion while Ghahremaninezhad and Ravi-Chandar (2013) have used a modified Arcan test to study the same Al 6061-T3.

One motivation for looking at failure under shear conditions is the slant type of fracture observed in the tearing of thin metallic sheets, where the final fracture surface often shows a void-sheet failure. Earlier studies (Saje et al., 1982; Tvergaard, 1989) relate to this type of situation, where typically failure occurs in a void-sheet under a positive stress triaxiality.

Deformation under low stress triaxiality can also be applied by subjecting the material to tensile loading in a fixed direction, with compressive loading in the transverse direction. Then material lines along these two loading directions do not rotate during the plastic deformations. When the hydrostatic tension is precisely zero, this mode of deformation is called pure shear. Tvergaard (2015a) recently studied a material containing a periodic array of voids subject to stress states in the vicinity of pure shear, using numerical solutions for a characteristic unit cell model. It was found that the voids close up to micro-cracks, but no failure mechanism was found and there were no maxima on the stress strain curves in pure shear. By a very different approach, using homogenisation theory for a ductile material, Song et al. (2015) also compared simple shear to pure shear. Their model does not account for contact when the

voids become micro-cracks, but for a high volume fraction they find localization in simple shear before the voids have closed up, while there is no localization in pure shear.

The void patterns considered in (Tvergaard, 2015a) maintain a high degree of symmetry during large deformations, but less symmetric imperfections could still result in failure. Therefore, the present study considers a single layer of voids in a ductile solid, which could initiate a shear localization leading to void-sheet failure, even though no failure in pure shear was predicted by Tvergaard (2015a) or Song et al. (2015).

2. PROBLEM FORMULATION AND NUMERICAL PROCEDURE

The initial imperfection in the material to be analysed here is represented by a row of uniformly spaced circular cylindrical holes with the radius R_0 and the spacing $2D_0$ (see Fig. 1), with the initial angle of inclination ψ_0 between the void-sheet and the x^1-axis. The block of material is assumed to be very large relative to the void spacing, and far away from the voids the principal true stresses are σ_1 and σ_2 in the x^1- and x^2-directions, respectively. The corresponding principal logarithmic strains in the far field are denoted ε_1 and ε_2, respectively. In the near vicinity of the void-sheet the stress and strain fields will differ significantly from the uniform far field, but at some distance from the row of voids there will be little difference.

The plane strain analyses here follow much of the formulations in Tvergaard (1989), mixed in with some of the formulations from Tvergaard (2012). Thus, a unit cell as that shown in Fig. 1 is drawn around each of the voids in the inclined void-sheet. All of these unit cells undergo identical deformations, and periodicity conditions apply along the sides of the unit cells. The initial width of the unit cell is $2A_0$ in the x^1-direction and the initial height is $2B_0$ in the x^2-direction, so that the half void spacing is $D_0 = A_0 / \cos\psi_0$. When the ratio B_0 / A_0 is chosen large enough, the stress and strain fields in the top and bottom parts of the unit cell will be practically identical to the far field, and this is used to define the loads on the unit cell. In most of the present analyses it is chosen to use $B_0 / A_0 = 2$.

Finite strains are accounted for, based on a convected coordinate Lagrangian formulation of the field equations, with a Cartesian x^i coordinate system used as reference and with the

displacement components on reference base vectors denoted by u^i. The metric tensors in the reference configuration and the current configuration, respectively, are g_{ij} and G_{ij} with determinants g and G, and $\eta_{ij} = 1/2\left(G_{ij} - g_{ij}\right)$ is the Lagrangian strain tensor. In terms of the displacement components u^i on the reference base vectors the Lagrangian strain tensor is

$$\eta_{ij} = \frac{1}{2}\left(u_{i,j} + u_{j,i} + u^k_{,i} u_{k,j}\right) \tag{1}$$

where $(\,)_{,j}$ denotes covariant differentiation in the reference frame. The contravariant components τ^{ij} of the Kirchhoff stress tensor on the current base vectors are related to the components of the Cauchy stress tensor σ^{ij} by $\tau^{ij} = \sqrt{G/g}\,\sigma^{ij}$. A finite strain formulation for a J_2 flow theory material with the Mises yield surface is applied, where the incremental stress-strain relationship takes the form $\dot{\tau}^{ij} = L^{ijk\ell}\dot{\eta}_{k\ell}$, with the instantaneous moduli specified in (Hutchinson, 1973; Tvergaard, 1976). The true stress-logarithmic strain curve in uniaxial tension is taken to follow the power law

$$\varepsilon = \begin{cases} \sigma/E, & \sigma \le \sigma_Y \\ (\sigma_Y/E)(\sigma/\sigma_Y)^{1/N}, & \sigma \ge \sigma_Y \end{cases} \tag{2}$$

with Young's modulus E, the initial yield stress σ_Y and the power hardening exponent N. Poisson's ratio is ν.

As in (Tvergaard, 2012) the corners of the unit cell are denoted A, B, C and D. When the top and bottom edges of the unit cell are assumed to satisfy compatibility and equilibrium with the far field, the current angle of inclination ψ of the void-sheet and the width of the unit cell are determined by the far field strains

$$\tan\psi = e^{(\varepsilon_2 - \varepsilon_1)} \tan\psi_0 \tag{3}$$

$$u^1_B - u^1_A = 2A_0(e^{\varepsilon_1} - 1) \tag{4}$$

$$u^2_B - u^2_A = 2A_0(e^{\varepsilon_1}\tan\psi - \tan\psi_0) \tag{5}$$

and it is assumed here that $u^1_A = u^2_A = 0$. Furthermore, compatibility requires that the displacements vary linearly along the edge AB

$$u^1(\eta_1) = u^1_A + (u^1_B - u^1_A)\eta_1/2D_0\,, \quad u^2(\eta_1) = u^2_A + (u^2_B - u^2_A)\eta_1/2D_0 \tag{6}$$

Equations analogous to (6) are also required for the edge DC, expressed in terms of the corner displacements u_D^i and u_C^i. Here, the two displacement components at D will be found from the two equilibrium requirements, and then the displacements at C are known, since the edge lines DC and AB are required to be parallel and have equal length.

Along the edge DC the requirement of equilibrium between the edge tractions T^i on the unit cell and the far field principal stresses can be written as

$$\int_0^{2D_0} T^2 d\eta_2 = \sigma_2(2A_0 + u_C^1 - u_D^1) \tag{7}$$

$$\int_0^{2D_0} T^1 d\eta_2 = -\sigma_1(2D_0 \sin\psi_0 + u_C^2 - u_D^2) \tag{8}$$

In the analyses, periodic boundary conditions are used on the unit cell model along the sides AD and BC to express compatibility and equilibrium with the neighbouring cells along the inclined row of voids. Thus, the following relations have to be satisfied between the displacements and the nominal tractions on the two sides

$$u^1(\xi_1) - u_A^1 = u^1(\xi_2) - u_B^1 \quad , \quad u^2(\xi_1) - u_A^2 = u^2(\xi_2) - u_B^2 \tag{9}$$

$$T^1(\xi_1) = -T^1(\xi_2) \quad , \quad T^2(\xi_1) = -T^2(\xi_2) \tag{10}$$

where ξ_1 and ξ_2 are length measuring coordinates defined in Fig. 1. A standard penalty method is used to approximately satisfy these periodic boundary conditions, as has been explained in detail in (Tvergaard, 2012).

The far field solution is taken to have a fixed ratio κ of the principal stresses, such that

$$\sigma_1 / \sigma_2 = \kappa \tag{11}$$

First the far field solution is determined, so that the values of principal logarithmic strains ε_1 and ε_2, and of σ_1, are known as functions of σ_2, and these values are used in Eqs. (3) to (8) at each stage of the incremental solution. For the unit cell an average logarithmic strain in the x^2-direction is calculated from the elongation of the cell-side AD as

$$\varepsilon_2^{av} = \ln\left(1 + (u_D^2 - u_A^2)/(2B_0)\right) \tag{12}$$

Since the strains in the cell far from the void will be close to those in the far field, and the material near the void will strain more, it is clear that ε_2^{av} will become larger than ε_2. If plastic flow localization occurs along the row of voids, the straining in the far field will stop, as elastic unloading occurs, and thus the ratio $d\varepsilon_2^{av} / d\varepsilon_2$ becomes infinite. For numerical

reasons a finite ratio, after that plastic yielding has initiated in the far field, is used here as the localization condition

$$d\varepsilon_2^{av} / d\varepsilon_2 > 10 \tag{13}$$

although this occurs slightly before the real localization.

When localization has occurred according to the condition (13), the computation is continued by specifying no further change in the far field, thus approximately representing elastic unloading in the far field. Instead, the average strain ε_2^{av} is increased incrementally, and the average tensile stress σ_2^{av} is calculated from the nodal forces on the edge DC.

Two different methods are considered here to approximately model crack surface contact and frictionless sliding that initiates when the void closes up in a micro-crack:

Method A is that proposed in Tvergaard (2009), where the length ℓ of the ellipsoidal cross-section of the void is calculated as the largest distance between two surface points, and the average width w of the void is calculated from the current void volume V_v per unit length in the x^3 direction as $w = V_v / \ell$. Then, instead of a detailed representation of crack surface contact as the void develops into a micro-crack, the approximation is made that the average aspect ratio of the void is required to satisfy the inequality

$$w / \ell \geq \rho \tag{14}$$

When the aspect ratio reaches the limit according to Eq. (14) an internal loading is applied to the void surface and this load is gradually increased so that the inequality (14) is not violated. Only traction components perpendicular to the line of length ℓ between the two end points of the void are applied, such that no load component will tend to increase the length of the void.

Method B makes use of individual nodal forces between nodes on either side of the crack. For each node the local opening w of the crack, normal to the line of length ℓ between end points, is calculated. If $w < w_c$ an opening force is applied to this nodal point and simultaneously two opening forces are applied to the two nearest nodes on the opposite side of the crack, such that these three forces are in self-equilibrium. Thus, in Method B the critical opening w_c is kept constant along the crack, except very near the crack-tips where a parabolic step down is used.

The numerical solutions are obtained by a linear incremental solution procedure, based on the incremental principle of virtual work. As in (Tvergaard, 2012) the displacement fields are approximated in terms of 8-noded isoparametric elements, and volume integrals in the

principle of virtual work are carried out by using 2×2 point Gauss integration within each element. Using the penalty method to approximately satisfy the periodic boundary conditions results in additional stiffness matrices, which are entered directly into the global stiffness matrix. An example of a mesh used for some of the numerical analyses is shown in Fig. 2.

Remeshing is used a few times in each computation to avoid severe mesh distortion, in particular where material flows around the sharp crack tips. The remeshing procedure applied was first introduced in one of the authors finite strain programmes by Pedersen (1998), and has been further developed in (Tvergaard 1997). The values of field quantities in the integration points of the new mesh are determined by interpolation in the old mesh. To do this, it is necessary to determine the location of each new nodal point and integration point in the old mesh, i.e. the element number and the appropriate values of the local coordinates ξ and η inside that element, where the region of the element is specified by $-1\le\xi\le1$ and $-1\le\eta\le1$. This is done by repeated use of a Newton-Raphson iteration.

3. RESULTS

In the computations to be presented here the material parameters are taken to be $\sigma_Y/E=0.002$, $\nu=0.3$ and $N=0.1$. Different values are considered for the initial void radius and the stress ratio κ in (11), while the initial aspect ratio of the region analysed is mostly taken to be $B_0/A_0=2$. The initial angle of inclination ψ_0 between the void-sheet and the x^1-axis is here taken to be 30^o because this was found in (Tvergaard, 1989) to be near the most critical angle for shear band localization along the row of voids. A few other values of ψ_0 will also be tested.

Fig. 3a shows the evolution of the principal stress σ_2 in the far field versus the average strain ε_2^{av} defined in (12), for $R_0/D_0=0.175$ and for different values of the stress ratio κ. Fig. 3b shows the corresponding evolution of the angle φ between the x^1-axis and the line of length ℓ connecting the two end points of the elongated void (see also Eq. (14)). Initially, while the void cross-section is circular, the value of the angle φ is not well defined, as is seen in Fig. 3b for small strains. For the three larger values of κ in Figs. 3a and 3b localization of plastic flow is predicted by reaching the condition (13). Thus, for $\kappa=0.0$, i.e. uniaxial plane strain tension, localization occurs at $\varepsilon_2^{av}=0.085$ (or at $\varepsilon_2=0.034$). For

$\kappa = -0.125$ localization occurs at $\varepsilon_2^{av} = 0.132$ (or at $\varepsilon_2 = 0.064$), while for $\kappa = -0.25$ localization occurs at $\varepsilon_2^{av} = 0.192$ (or at $\varepsilon_2 = 0.110$). In the remaining three cases contact between the crack surfaces initiates before any localization has been predicted, and no subsequent localization is predicted either while the material deforms around the closed cracks. For $\kappa = -1.0$, i.e. for pure shear, contact initiates near the point $\varepsilon_2^{av} = 0.168$ (or $\varepsilon_2 = 0.140$), while for $\kappa = -0.75$ contact initiates near $\varepsilon_2^{av} = 0.187$ (or $\varepsilon_2 = 0.152$), and for $\kappa = -0.5$ contact initiates near $\varepsilon_2^{av} = 0.218$ (or $\varepsilon_2 = 0.167$). Contact is here modelled using the Method B described below Eq. (14). It is noted in Fig. 3a that the curves for the three larger values of κ have reached a stress maximum, corresponding to the prediction of material failure, whereas on the other three curves, where no localization is predicted, the stress keeps growing with increasing strain.

In relation to Fig. 3b it is noted that $\varphi = 90^o$ would be the result if there was no influence of the gradually increasing shearing around the imperfection represented by the inclined row of voids. Thus for $\psi_0 = 0^o$ there would be no imperfection to initiate shearing, and the void axis would remain parallel to the x^2-axis ($\varphi = 90^o$). In Fig. 3b, where the inclined imperfection creates a band of increasing shearing, it is seen that the elongated voids rotate clockwise in this band, such that the values of the angle φ decay as the tensile strain is increased. This reduction of φ is most pronounced for $\kappa = 0.0$, where plastic flow localization occurs first, but it is also clear for the two other cases, where localization in a shear band is predicted.

The curve for $\kappa = -1.0$ in Fig. 3b shows that, as for the other curves, the value of the angle φ decays as the strain is increased, but this stops at the point where crack surface contact initiates, and afterwards the micro-crack rotates backwards towards the value 90^o. The curve for $\kappa = -0.75$ behaves the same way, except that here the change to anti-clockwise rotation occurs a little later, because the initiation of crack surface contact occurs a little later. For $\kappa = -0.5$ the change to a growing value of the angle φ is just occurring at the end of the curve shown in Fig. 3b, since this is where contact initiates.

The purpose of the present investigation is to see if a less symmetric imperfection than those considered in (Tvergaard, 2015a) could still result in failure under pure shear conditions. The inclined layer of voids is considered here, because it is known from (Tvergaard, 1989) that this imperfection can initiate shear localization leading to void-sheet

failure, and indeed such void-sheet failure is predicted in Fig. 3 for the three larger values of κ. But Fig. 3 also shows that for stress states close to pure shear this development towards shear failure is interrupted when the voids close up to form micro-cracks. Thus the present studies support the conclusion in (Tvergaard, 2015a) that no failure and no stress maximum is predicted for stress states near pure shear.

A plot of the normalized average strain $\varepsilon_2^{av}/\varepsilon_2$ vs. ε_2 is shown in Fig. 4 for the cases also illustrated in Fig. 3. For $\kappa = 0.0$ and the two curves closest to this case the slope grows very large at the end, indicating that the average strain in the cell keeps growing while straining stops in the infinite solid outside the cell, as is typical for plastic strain localization developing from an initial imperfection. The other three curves, for stress states closer to pure shear, show no such tendency towards localization. Thus, Fig. 4 confirms the conclusions drawn on the basis of Fig. 3.

Fig. 5 shows the deformed unit cell with contours of effective plastic strain at three stages of the computation for $\kappa = -1.0$ in Fig. 3. In Fig. 5a, at $\varepsilon_2^{av} = 0.135$ and $\varphi = 78.6^o$, the void surfaces are not yet in contact, and the elongated void is still rotating in the clockwise direction. In Fig. 5b, at $\varepsilon_2^{av} = 0.184$, contact has occurred while the angle of orientation of the crack passed a minimum of 77.3^o, but the value of the angle has now again increased to $\varphi = 79.0^o$. At the last stage reached in this computation, Fig. 5c at $\varepsilon_2^{av} = 0.261$, the value of the angle has grown to $\varphi = 84.4^o$, as was also seen on the curve in Fig. 3b. In Fig. 5a it is clear that a band of more intense straining has developed along the inclined row of voids. In Fig. 5c this band of more intense straining is still visible, but it has not developed towards a stronger localization, since both the strains inside the band and those outside have increased by about the same amount. This is also seen from the fact that the difference between the average strain and the far field strain, $\varepsilon_2^{av} - \varepsilon_2$, has not increased.

In real materials there is often a particle inside the voids, and analyses have shown that this plays a role by not allowing the voids to collapse (Tvergaard, 1989; Siruguet and Leblond, 2004). In the present studies with large transverse compression and large void elongation there would be both regions of contact to the inclusion and regions of contact between adjacent void surfaces. Due to this more complex contact situation the inclusions have been neglected in the present studies.

The boundary conditions (3) to (8) are formulated such that the behavior of the voids will depend only on the evolution of the far field stress and strain history, but not on the

chosen value of the unit cell aspect ratio B_0 / A_0 if this ratio is chosen large enough, since then the stress and strain fields in the cell far from the void will essentially coincide with the far field. To test this, the computation for $\kappa = -1.0$ illustrated in Figs. 3 and 5 has been compared with a similar computation using the double value of the unit cell aspect ratio, $B_0 / A_0 = 4$. The evolution of the stress σ_2 and the angle φ are compared in Figs. 6a and 5b as functions of the far field strain ε_2, since it is the dependence on the far field that should be independent of the unit cell aspect ratio. In Fig. 6a the two curves coincide, as expected since both quantities belong to the far field, but it is noted that due to Eq. (7) σ_2 is also the average tensile stress in the unit cell. Fig. 6b shows that the values of the angle φ differ only little between the two computations, the trends in the evolution are the same, including the change from a decaying angle to an increasing angle near the points where void surface contact initiates. If the evolution of φ had been plotted against the average strain ε_2^{av}, as in Fig. 3b, the agreement would not be as good, since the ratio $\varepsilon_2^{av} / \varepsilon_2$ is larger for smaller values of the aspect ratio B_0 / A_0 due to the increased strain level in the local region around the void.

The length of the void or micro-crack ℓ, used in Eq. (14), has the initial value $2R_0$ for a circular cylindrical void, and thus the initial value of the ratio ℓ / D_0 is 0.35 in the computations of Fig. 6. At the end of the computation for $B_0 / A_0 = 4$ in Fig. 6, where $\varepsilon_2 = 0.223$, the normalized length is $\ell / D_0 = 0.629$, while the value is $\ell / D_0 = 0.622$ in the computation for $B_0 / A_0 = 2$ at $\varepsilon_2 = 0.223$. Thus, not only the evolution of the angle φ as a function of ε_2, as shown in Fig. 6b, but also the corresponding growth of the micro-crack length ℓ appear to be rather independent of the unit cell aspect ratio B_0 / A_0, as long as this ratio is not too small.

As mentioned above, the initial angle of inclination ψ_0 between the row of voids and the x^1-axis has been taken to be 30^o because this was found (Tvergaard, 1989) to be near the most critical angle for shear band localization. A few computations with different values of the angle are carried out here to check the dependence on ψ_0 in a case like that for $\kappa = -1.0$ in Figs. 3 and 5, where shear band localization does not occur. Fig. 7a shows that the levels of the stress vs. strain curves are not very sensitive to the value of ψ_0, and near the end where void surface contact has occurred the stress levels are nearly identical. Fig. 7b shows much

more difference. For $\psi_0 = 20^o$ there is very little tendency towards shearing along the row of voids (nothing like that shown in Fig. 5a), and the value of the angle φ remains nearly constant, around 88^o. On the other hand, for $\psi_0 = 40^o$ there is significant shearing initially, leading to a clear reduction of the angle φ, but then void surface contact initiates rather early and the value of φ grows back towards 90^o. When comparing to the full curve for $\psi_0 = 30^o$, the curves corresponding to the two other angles of inclination are closer to 90^o at larger strains, so it appears that these cases were less close to reach a localization before this tendency was stopped by the occurrence of void surface contact.

While all other computations in the present paper have used method B to approximately represent the void surface contact when the voids collapse to a micro-crack, one computation for $\psi_0 = 30^o$ and $\kappa = -1.0$ has been carried out using method A, as described around Eq. (14), with $\rho = 0.15$. This computation is illustrated by the dotted curves in Fig. 7, where the full curves illustrate exactly the same case with the only difference that contact is approximated by method B. In Fig. 7a the two curves are practically indistinguishable, and in Fig. 7b they are very close both before and after the onset of contact. The deformed meshes at the end of these two computations are shown in Fig. 8. It is noted that method A, which has been used in a number of previous investigations (Tvergaard, 2009, 2012), prescribes only an average opening of the micro-crack, while method B attempts to keep the opening constant along the crack. Anyway, the comparison in Fig. 7 shows that the results obtained by these two approximations are very similar.

The effect of the hardening exponent N is considered in Fig. 9 for the case of pure shear, $\kappa = -1.0$. As expected (Fig. 9a), the more high hardening material, $N = 0.2$, gives higher stress levels, while low hardening gives lower stress, but none of the curves reach zero slope as no localization is predicted. Fig. 9b shows that the minimum, where micro-crack closure initiates, occurs a bit later for the high hardening material and earlier for the low hardening material. At all three hardening levels the elongated voids first rotate in the clockwise direction, with the shearing, but after crack closure the micro-cracks rotate back in the anticlockwise direction.

The void spacing considered here may seem small relative to the void radius, but it should be recalled that the void volume fraction in these analyses is essentially zero, because the strip of material represented by the unit cell is connected to the infinite void free material

through the boundary conditions (3)-(8). Thus, the particular imperfection considered here is a special cluster in the form of a single row of voids.

To check the influence of the void size, curves like those in Fig. 3 have also been computed for other values of the R_0 / D_0 . Fig. 10 shows results for $R_0 / D_0 = 0.25$, with no other parameters changed relative to those used in the computations illustrated in Fig. 3. The main difference from Fig. 3 is that also the computation for $\kappa = -0.5$ leads to the prediction of localization in a shear band. Furthermore, the four cases that result in localization in Fig. 10 show generally larger rotations of the voids in the shear field that develops along the row of voids (i.e. smaller values of φ), so it is clear that the stronger imperfection represented by the larger voids amplifies the tendency to reach a final void-sheet failure. In the two remaining cases, for pure shear or near pure shear, void surface contact occurs and subsequently the shear rotation of the voids is terminated so that no localization occurs, as was also found in Fig. 3.

Again in Fig. 11 the only difference from the cases considered in Figs. 3 and 10 is the relatively smaller voids, $R_0 / D_0 = 0.125$. Here, localization is predicted only for the two larger values of κ. For the case $\kappa = -0.25$ void surface contact has initiated a little before the end of the curves shown, so here is not going to be localization. The curves for the three smaller values of κ show clearly a minimum in Fig. 11b, so that the value of the angle φ again starts to increase while the deformations continue with crack surface contact.

Among the six different values of κ considered in Figs. 3, 10 and 11 it is seen that plastic flow localization is predicted for four of the values in the case of the strongest imperfection (Fig. 10), for three of the values in the case of the intermediate imperfection (Fig. 3), and only for two of the values in the case of the smallest imperfection (Fig. 11). But the common picture is that no localization has been found for pure shear or for the near vicinity of pure shear.

4. DISCUSSION

The analyses in the present paper have been carried out to further study the possibility of failure in a porous ductile material under conditions of pure shear. At zero stress triaxiality it has been found that for simple shear a maximum shear stress is reached with subsequent failure prediction (Tvergaard, 2009, 2012; Dahl et al., 2012), whereas for pure shear no stress

maximum was reached and no instability was detected (Tvergaard, 2015a). Both in simple shear and in pure shear it has been found that the voids close up to micro-cracks early on, and the failures predicted in simple shear involve the interaction of such micro-cracks, which rotate and elongate during continued shear deformations. Even though a bifurcation into a shear band was not found in the study of pure shear, there is the possibility that a shear band instability could develop from an initial imperfection that would gradually amplify an inclined shear zone in the material.

The initial imperfection chosen here is an inclined row of voids, since it has been found in a number of previous studies that under moderate or higher stress triaxiality this type of imperfection will lead to shear localization and final void-sheet failure in the shear band. Indeed, the present results show that shear localization is predicted for moderate stress triaxiality corresponding to uniaxial plane strain tension, and even for a range of smaller stress triaxialities than that. But for pure shear, with zero stress triaxiality, and for a range of low stress triaxialities near pure shear no shear localization and no stress maximum are found. As expected a larger imperfection, i.e. a larger ratio of the void radius to void spacing, increases the stress range where localization is predicted, but even for the largest imperfection considered here there is no localization prediction in the near vicinity of pure shear. For the smallest imperfection considered localization predictions are limited to stress states near uniaxial plane strain tension or higher stress triaxialities.

It may be claimed that under the large transverse compressive stresses in pure shear the collapsed voids are pressed together so effectively that even physical intuition would say that there could be no failure, and this was part of the argument in the Discussion of (Tvergaard, 2015a). But it is known from previous studies of shear band instabilities that there is often a significant imperfection sensitivity, and therefore the present study has focused on a rather strong imperfection of the type that could trigger shear bands, in order to see if this would lead to a failure prediction.

A plane strain programme is used for the present analyses, which cannot account for the 3D effects associated with spherical voids. Some impression of the approximation involved in a plane strain analysis with cylindrical voids can be obtained from the analyses of Nielsen et al. (2012) for simple shear. There, a comparison of spherical voids and cylindrical voids has shown that for the same local void volume fraction earlier failure is predicted by cylindrical voids, but not much earlier. Thus, it can be expected that the same local void volume fraction of spherical voids inside the void-sheet would give localization a little later than predicted for

cylindrical voids. Even with some random distribution of such spherical voids in the void-sheet the behavior is not expected to differ much from uniformly spaced spherical voids, as long as voids have not started to coalesce.

Initially flat or elongated cylindrical voids could also be of interest. A recent study for such void shapes under simple shear (Tvergaard, 2015b) has shown that during deformation the voids develop into shapes very similar to those resulting from voids that are initially circular cylindrical.

It should be emphasized that the results obtained here are relevant to J_2 flow theory. As was discussed in (Tvergaard, 2015a) the predictions would be very different if formation of a vertex on the yield surface was assumed, as described by J_2 corner theory (Christoffersen and Hutchinson, 1979). Then shear band localization would occur early (Hill and Hutchinson, 1975), and for $N = 0.1$ the critical strain would be around 0.3 (Hutchinson and Tvergaard, 1981), also in pure shear. Not only the present studies but practically all studies of void growth and void interaction would be strongly affected by an assumption that the material forms a vertex on the yield surface, since large strains usually develop, so that rather early loss of ellipticity would be predicted in the material near voids.

Recent experimental results for an Aluminium alloy (Morgeneyer et al., 2014), based on in situ 3D tomography/laminography, have shown that shear localization can occur prior to voiding, while voids later grow in the band to give failure. This early localization may be due to a vertex on the yield surface, as would also be predicted by crystal plasticity, but even though a number of alloys do show a vertex type of response (Hecker, 1976), it requires a test to show that for a particular material.

The method used in the present analyses is different from that used in (Tvergaard, 2015a), but the results confirm those obtained previously, where no maximum stress was reached and no shear band instability was found in pure shear. The imperfection considered in the present study does initiate a band of extra shearing along the inclined row of voids, but for stress states corresponding to pure shear, or near pure shear, the voids collapse to micro-cracks before localization is predicted, and subsequently no localization occurs. As long as the extra shearing develops along the imperfection, the elongated voids rotate in the shear direction, but after that void surface contact has occurred the micro-cracks start to rotate in the opposite direction, approaching a situation where the cracks are aligned with the principal tensile stress, i.e. a situation similar to that considered by (Tvergaard, 2015a). Thus, even with

an imperfection designed to promote shear fracture no failure is predicted here under pure shear.

While in the present analyses of pure shear the tendency towards shear localization is interrupted by voids collapsing to micro-cracks, it is noted that in the previous studies of simple shear, or stress states near simple shear, the voids have collapsed to micro-cracks before a maximum shear stress is reached and failure is predicted (Tvergaard, 2009, 2012). An important difference seems to be that in simple shear neighbouring micro-cracks keep rotating towards each other while they elongate and develop an increasing overlap, which develops into micro-crack coalescence.

The pure shear stress state with axial tension and transverse compression is somewhat similar to that under rolling with big roller diameters, if the plate subject to rolling is simultaneously under axial tension. Since very large strains can be sustained in rolling without any material failure, it is perhaps not surprising that no failure is predicted in the present analyses for pure shear. Also in some forging operations pure shear can occur. On the other hand, the stress state in simple shear is much like that in a tube under torsion, where failure has been predicted in a number of different investigations.

REFERENCES

Bao, Y., Wierzbicki, T. (2004) On fracture locus in the equivalent strain and stress triaxiality space, International Journal of Mechanical Sciences, 46:81-98.

Barsoum, I., Faleskog, J. (2007a) Rupture mechanisms in combined tension and shear – Micromechanics. Int. J. Solids Struct. 44:5481-5498.

Barsoum, I., Faleskog, J. (2007b) Rupture mechanisms in combined tension and shear – Experiments. Int. J. Solids Struct. 44:1768-1786.

Barsoum, I., Faleskog, J. (2011) Micromechanical analysis on the influence of the Lode parameter on void growth and coalescence. Int. J. Solids Struct. 48:925-938.

Beese, A.M., Luo, M., Li, Y., Bai, Y., Wierzbicki, T. (2010) Partially coupled anisotropic fracture model for aluminum sheets, Engineering Fracture Mechanics, 77:1128-1152.

Benzerga, A.A., Leblond, J.-B. (2010) Ductile fracture by void growth to coalescence. Advances in Applied Mechanics, 44:169-305. Dahl, J., Nielsen, K.L., Tvergaard, V. (2012) Effect of contact conditions on void coalescence at low stress triaxiality shearing. J. Appl. Mech., ASME 79, Issue 2: Art. No. 021003.

Christoffersen, J. and Hutchinson, J.W. (1979) A class of phenomenological corner theories of plasticity. J. Mech. Phys. Solids 27:465-487.

Dahl, J., Nielsen, K.L., Tvergaard, V. (2012) Effect of contact conditions on void coalescence at low stress triaxiality shearing. J. Appl. Mech., ASME 79, Issue 2: Art. No. 021003.

Dunand, M., Mohr, M. (2011) Optimized butterfly specimen for the fracture testing of sheet materials under combined normal and shear loading, Engineering Fracture Mechanics, 78:2919-2934.

Garrison Jr, W.M., Moody, N.R. (1987) Ductile fracture. J. Phys. Chem. Solids 48(11):1035-1074.

Ghahremaninezhad, A., Ravi-Chandar, K. (2013) Ductile failure in polycrystalline aluminum alloy Al 6061-T6 under shear dominant loading, International Journal of Fracture, 180:23-39.

Haltom, S.S., Kyriakides, S., Ravi-Chandar, K. (2013) Ductile failure under combined shear and tension, International Journal of Solids and Structures, 50:1507-1522.

Hecker, S.S. (1976) Experimental studies of yield phenomena in biaxially loaded metals. In Constitutive Equations in Viscoplasticity, ASME AMD, 20, 1-33.

Hill, R. and Hutchinson, J.W. (1975) Bifurcation phenomena in the plane tension test. J. Mech. Phys. Solids 23:239-264.

Hutchinson, J.W. (1973) Finite strain analysis of elastic-plastic solids and structures. In: Hartung, R.F. (Ed.), Numerical Solution of Nonlinear Structural Problems. ASME, New York, p. 17.

Hutchinson, J.W., Tvergaard, V. (1981) Shear band formation in plane strain. Int. J. Solids Structures 17:451-470.

Morgeneyer, T.F., Taillandier-Thomas, T., Helfen, L., Baumbach, T., Sinclair, I., Toux, S. and Hild, F. (2014) In situ 3-D observation of early strain localization during failure of thin Al alloy (2198) sheet. Acta Materialia 69, 78-91.

Nielsen, K.L., Dahl, J. and Tvergaard, V. (2012) Collapse and coalescence of spherical voids subject to intense shearing: Studied in full 3D. Int. J. Fracture 177:97-108.

Pedersen, T.Ø. (1998) Remeshing in analysis of large plastic deformations. Computers and Structures 67:279-288.

Rogers, H.C. (1960) The tensile fracture of ductile metals. Trans. Metal. Soc AIME 218, 498-506.

Saje, M., Pan, J., Needleman (1982) Void nucleation effects on shear localization in porous plastic solids. Int. J. Fracture 19, 163-182.

Siruguet, K. and Leblond, J.-B. (2004) Effect of void locking by inclusions upon the plastic behavior of porous ductile solids – I: theoretical modeling and numerical study of void growth. Int. J. Plasticity 20, 225-254.

Song, D., Agoras, M. and Ponte Castañeda, P. (2015) The evolution of pore shape and orientation in plastically deforming metals: implications for macroscopic response and shear localization. Mechanics of Materials. (in Press).

Tekoglu, C., Hutchinson, J.W., Pardoen, T. (2014) On localization and void coalescenceas a precursor to ductile fracture. (to appear)

Tvergaard, V. (1976) Effect of thickness inhomogeneities in internally pressurized elastic-plastic spherical shells. J. Mech. Phys. Solids 24:291.

Tvergaard, V. (1981). Influence of voids on shear band instabilities under plane strain conditions. *Int. J. Fracture* 17, 389-407.

Tvergaard, V. (1982) Ductile fracture by cavity nucleation between larger voids. *J. Mech. Phys. Solids* 30, 265-286.

Tvergaard, V. (1989) Numerical study of localization in a void-sheet. *Int. J. Solids Structures* 25, 1143-1156.

Tvergaard, V. (1990) Material failure by void growth to coalescence. Advances in Applied Mechanics 27:83-151.

Tvergaard, V. (1997) Studies of void growth in a thin ductile layer between ceramics, Computational Mechanics 20:186-191.

Tvergaard, V. (2008) Shear deformation of voids with contact modeled by internal pressure. Int. J. Mech. Sci. 50:1459-1465.

Tvergaard, V. (2009) Behaviour of voids in a shear field. Int. J. Fracture 158:41-49.

Tvergaard, V. (2012) Effect of stress-state and spacing on voids in a shear-field. Int. J. Solids Structures 49:3047-3054.

Tvergaard, V. (2015a) Behaviour of porous ductile solids at low stress triaxiality in different modes of deformation. Int. J. Solids Structures 60-61:28-34.

Tvergaard, V. (2015b) Effect of initial void shape on ductile failure in a shear field. Mechanics of Materials (in press).

Yamamoto, H. (1978) Conditions for shear localization in ductile fracture of void containing materials. Int. J. Fracture14:347-365.

Figure captions:

Fig.1. A unit cell used to analyze a material with a row of uniformly spaced circular cylindrical holes with initial radius R_0 and spacing $2D_0$. The initial angle of inclination between the void-sheet and the x^1-axis is ψ_0.

Fig. 2. Example of a mesh used for the numerical analysis.

Fig. 3a. Curves of the true tensile stress σ_2 in the far field vs. the average logarithmic strain ε_2^{av}, for $B_0 / A_0 = 2$, $R_0 / D_0 = 0.175$ and various values of $\sigma_1 / \sigma_2 = \kappa$.

Fig. 3b. Curves of the angle φ between the x^1-axis and the axis of the elongated void vs. the average logarithmic strain ε_2^{av}, for $B_0 / A_0 = 2$, $R_0 / D_0 = 0.175$ and various values of $\sigma_1 / \sigma_2 = \kappa$.

Fig. 4. Curves of the ratio $\varepsilon_2^{av} / \varepsilon_2$ vs the remote logarithmic strain ε_2, for $B_0 / A_0 = 2$, $R_0 / D_0 = 0.175$ and various values of $\sigma_1 / \sigma_2 = \kappa$.

Fig. 5ab. Deformed unit cells with contours of effective plastic strain corresponding to the computation with $\kappa = -1.0$, $B_0 / A_0 = 2$ and $R_0 / D_0 = 0.175$ in Fig. 3. (a) At $\varepsilon_2^{av} = 0.135$. (b) At $\varepsilon_2^{av} = 0.184$.

Fig. 5c. Deformed unit cell with contours of effective plastic strain corresponding to the computation with $\kappa = -1.0$, $B_0 / A_0 = 2$ and $R_0 / D_0 = 0.175$ in Fig. 3. (c) At $\varepsilon_2^{av} = 0.261$.

Fig. 6a. Curves of the true tensile stress σ_2 in the far field vs. the far field logarithmic strain ε_2, for $R_0 / D_0 = 0.175$, $\kappa = -1.0$ and either $B_0 / A_0 = 2$ or $B_0 / A_0 = 2$.

Fig. 6b. Curves of the angle φ between the x^1-axis and the axis of the elongated void vs. the far field logarithmic strain ε_2, for $R_0 / D_0 = 0.175$, $\kappa = -1.0$ and either $B_0 / A_0 = 2$ or $B_0 / A_0 = 2$.

Fig. 7a. Curves of the true tensile stress σ_2 in the far field vs. the average logarithmic strain ε_2^{av}, for $B_0 / A_0 = 2$, $R_0 / D_0 = 0.175$ and $\kappa = -1.0$. Curves are shown for $\psi_0 = 20^o$ and for $\psi_0 = 40^o$, while the other two curves have $\psi_0 = 30^o$. One curve is based on contact method A, while the other three curves are based on method B.

Fig. 7b. Curves of the angle φ between the x^1-axis and the axis of the elongated void vs. the average logarithmic strain ε_2^{av}, for $B_0 / A_0 = 2$, $R_0 / D_0 = 0.175$ and $\kappa = -1.0$. Curves are shown for $\psi_0 = 20^o$ and for $\psi_0 = 40^o$, while the other two curves have $\psi_0 = 30^o$. One curve is based on contact method A, while the other three curves are based on method B.

Fig. 8. Deformed meshes at the end of two different computations with $\kappa = -1.0$, $B_0 / A_0 = 2$ and $R_0 / D_0 = 0.175$. (a) Contact method B, at $\varepsilon_2^{av} = 0.261$. (b) Contact method A, at $\varepsilon_2^{av} = 0.275$.

Fig. 9a. Curves of the true tensile stress σ_2 in the far field vs. the average logarithmic strain ε_2^{av}, for $B_0 / A_0 = 2$, $R_0 / D_0 = 0.175$, $\kappa = -1.0$ and various values of the hardening exponent N.

Fig. 9b. Curves of the angle φ between the x^1-axis and the axis of the elongated void vs. the average logarithmic strain ε_2^{av}, for $B_0 / A_0 = 2$, $R_0 / D_0 = 0.175$, $\kappa = -1.0$ and various values of the hardening exponent N.

Fig. 10a. Curves of the true tensile stress σ_2 in the far field vs. the average logarithmic strain ε_2^{av}, for $B_0 / A_0 = 2$, $R_0 / D_0 = 0.25$ and various values of $\sigma_1 / \sigma_2 = \kappa$.

Fig. 10b. Curves of the angle φ between the x^1-axis and the axis of the elongated void vs. the average logarithmic strain ε_2^{av}, for $B_0 / A_0 = 2$, $R_0 / D_0 = 0.25$ and various values of $\sigma_1 / \sigma_2 = \kappa$.

Fig. 11a. Curves of the true tensile stress σ_2 in the far field vs. the average logarithmic strain ε_2^{av}, for $B_0 / A_0 = 2$, $R_0 / D_0 = 0.125$ and various values of $\sigma_1 / \sigma_2 = \kappa$.

Fig. 11b. Curves of the angle φ between the x^1-axis and the axis of the elongated void vs. the average logarithmic strain ε_2^{av}, for $B_0 / A_0 = 2$, $R_0 / D_0 = 0.125$ and various values of $\sigma_1 / \sigma_2 = \kappa$.

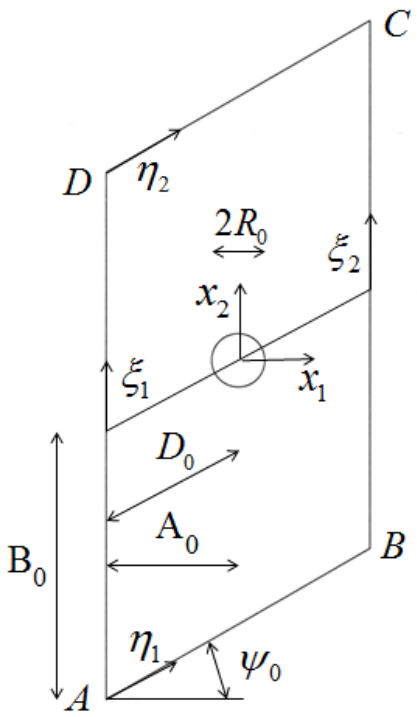

Fig.1. A unit cell used to analyze a material with a row of uniformly spaced circular cylindrical holes with initial radius R_0 and spacing $2D_0$. The initial angle of inclination between the void-sheet and the x^1-axis is ψ_0.

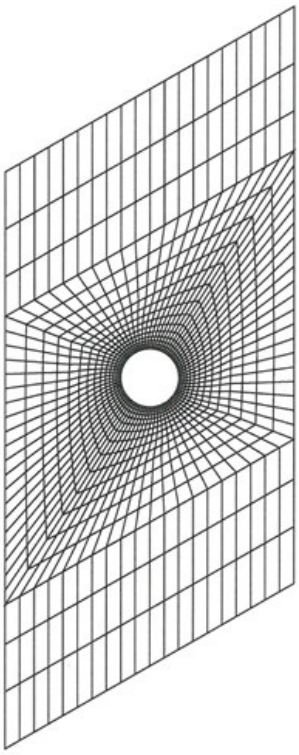

Fig. 2. Example of a mesh used for the numerical analysis.

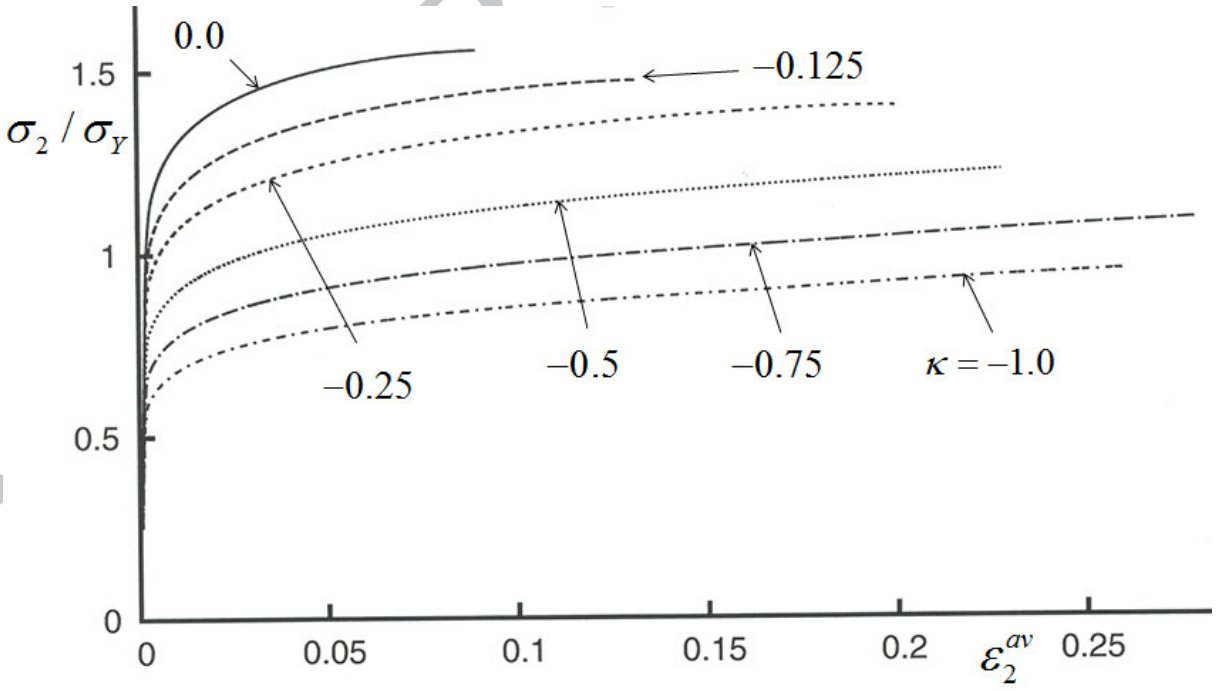

Fig. 3a. Curves of the true tensile stress σ_2 in the far field vs. the average logarithmic strain ε_2^{av}, for $B_0 / A_0 = 2$, $R_0 / D_0 = 0.175$ and various values of $\sigma_1 / \sigma_2 = \kappa$.

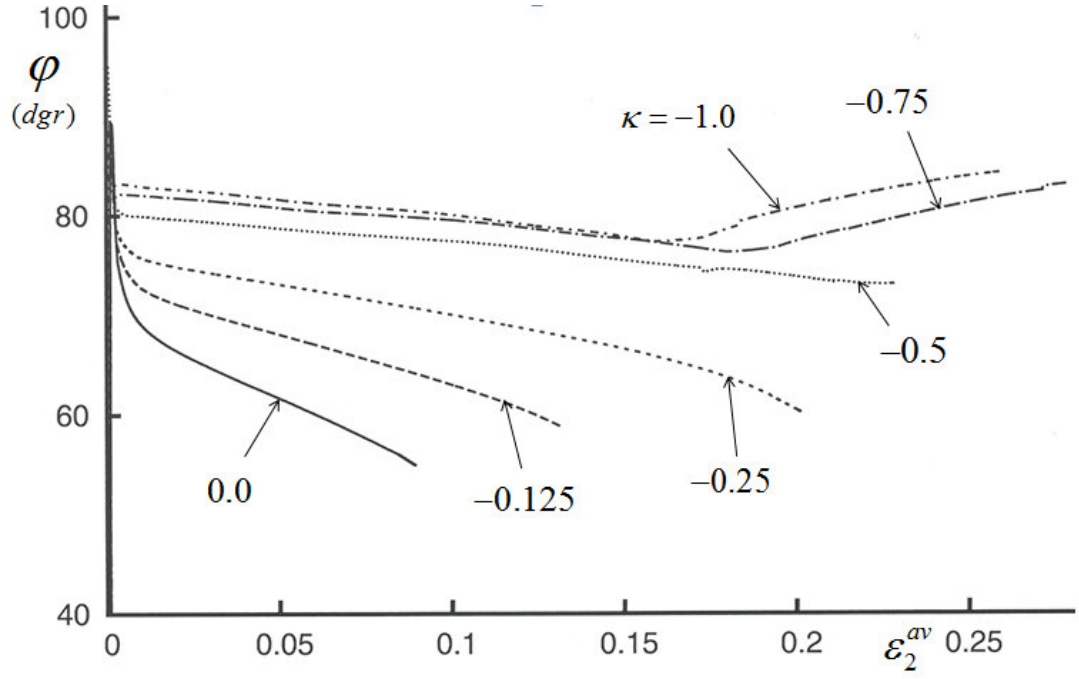

Fig. 3b. Curves of the angle φ between the x^1-axis and the axis of the elongated void vs. the average logarithmic strain ε_2^{av}, for $B_0 / A_0 = 2$, $R_0 / D_0 = 0.175$ and various values of $\sigma_1 / \sigma_2 = \kappa$.

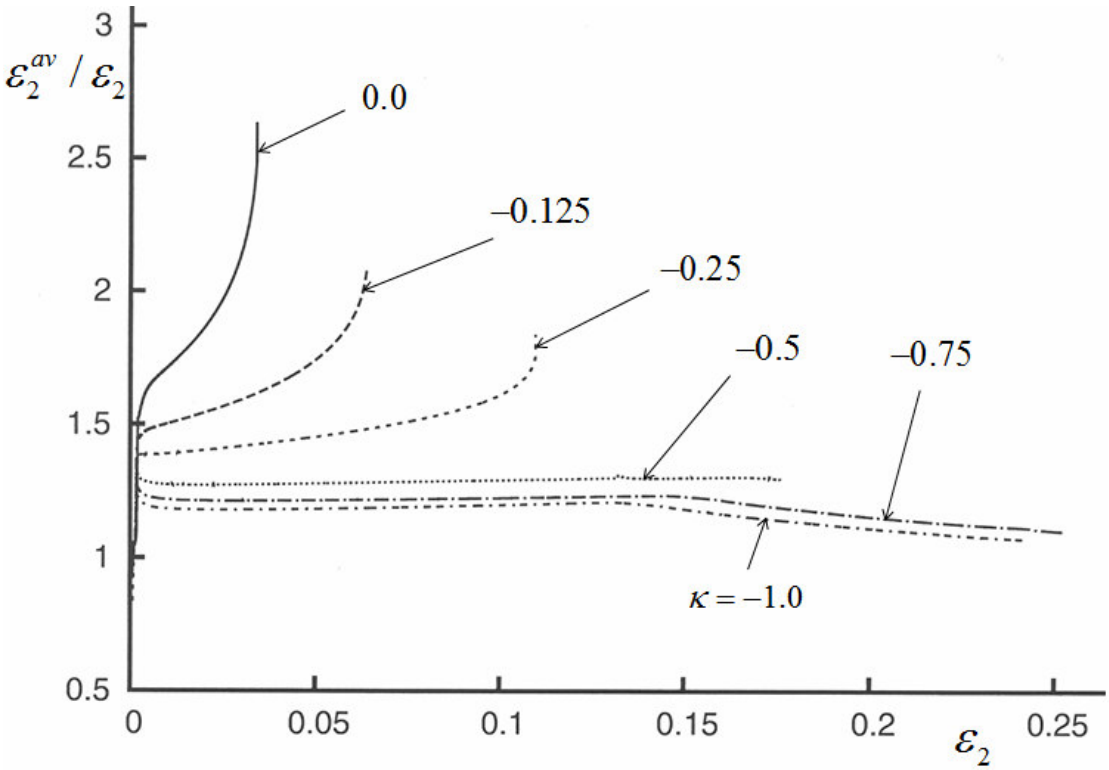

Fig. 4. Curves of the ratio $\varepsilon_2^{av} / \varepsilon_2$ vs the remote logarithmic strain ε_2, for $B_0 / A_0 = 2$, $R_0 / D_0 = 0.175$ and various values of $\sigma_1 / \sigma_2 = \kappa$.

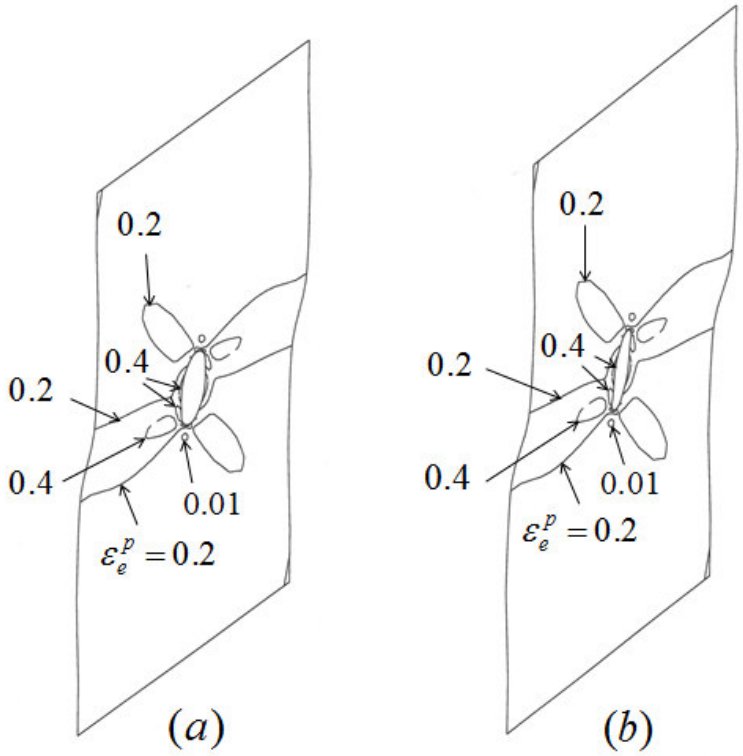

Fig. 5ab. Deformed unit cells with contours of effective plastic strain corresponding to the computation with $\kappa = -1.0$, $B_0 / A_0 = 2$ and $R_0 / D_0 = 0.175$ in Fig. 3. (a) At $\varepsilon_2^{av} = 0.135$. (b) At $\varepsilon_2^{av} = 0.184$.

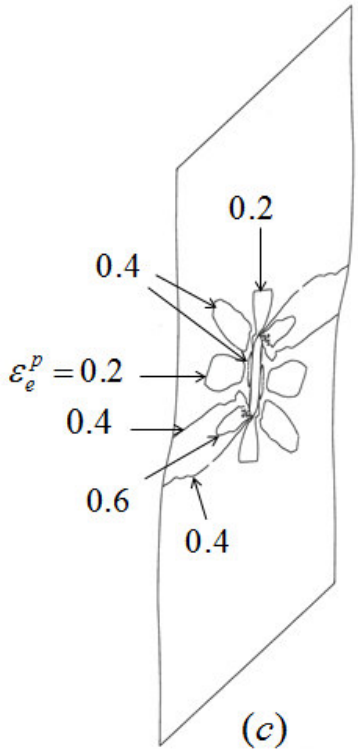

Fig. 5c. Deformed unit cell with contours of effective plastic strain corresponding to the computation with $\kappa = -1.0$, $B_0 / A_0 = 2$ and $R_0 / D_0 = 0.175$ in Fig. 3. (c) At $\varepsilon_2^{av} = 0.261$.

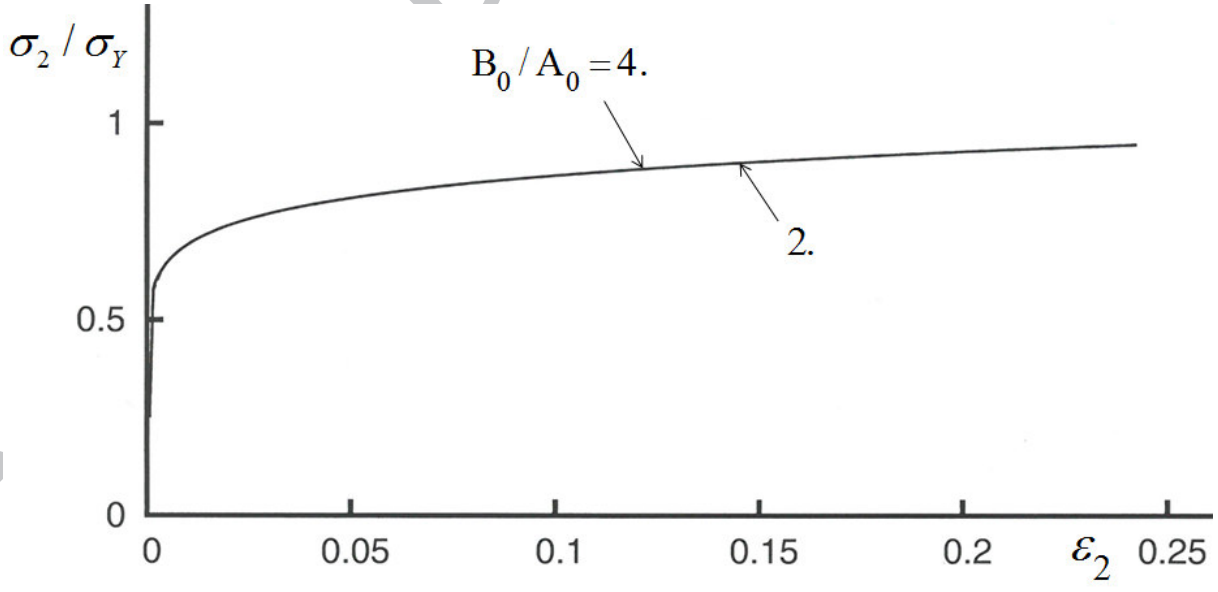

Fig. 6a. Curves of the true tensile stress σ_2 in the far field vs. the far field logarithmic strain ε_2, for $R_0 / D_0 = 0.175$, $\kappa = -1.0$ and either $B_0 / A_0 = 2$ or $B_0 / A_0 = 2$.

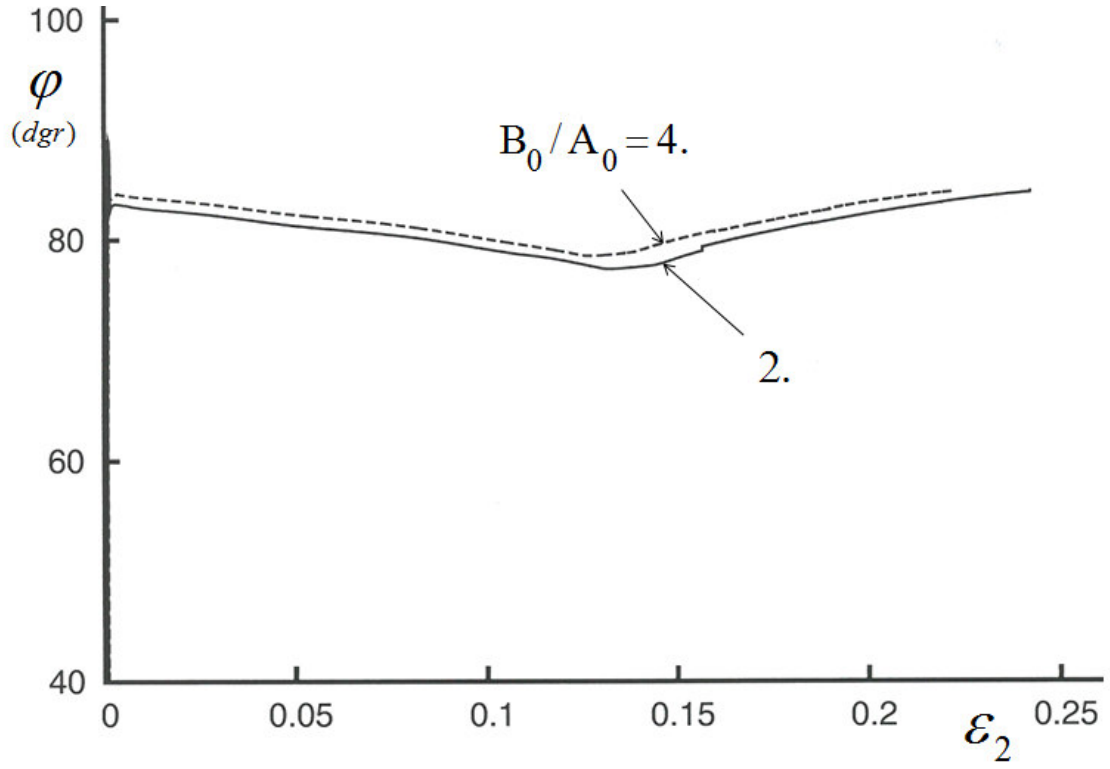

Fig. 6b. Curves of the angle φ between the x^1-axis and the axis of the elongated void vs. the far field logarithmic strain ε_2, for $R_0 / D_0 = 0.175$, $\kappa = -1.0$ and either $B_0 / A_0 = 2$ or $B_0 / A_0 = 2$.

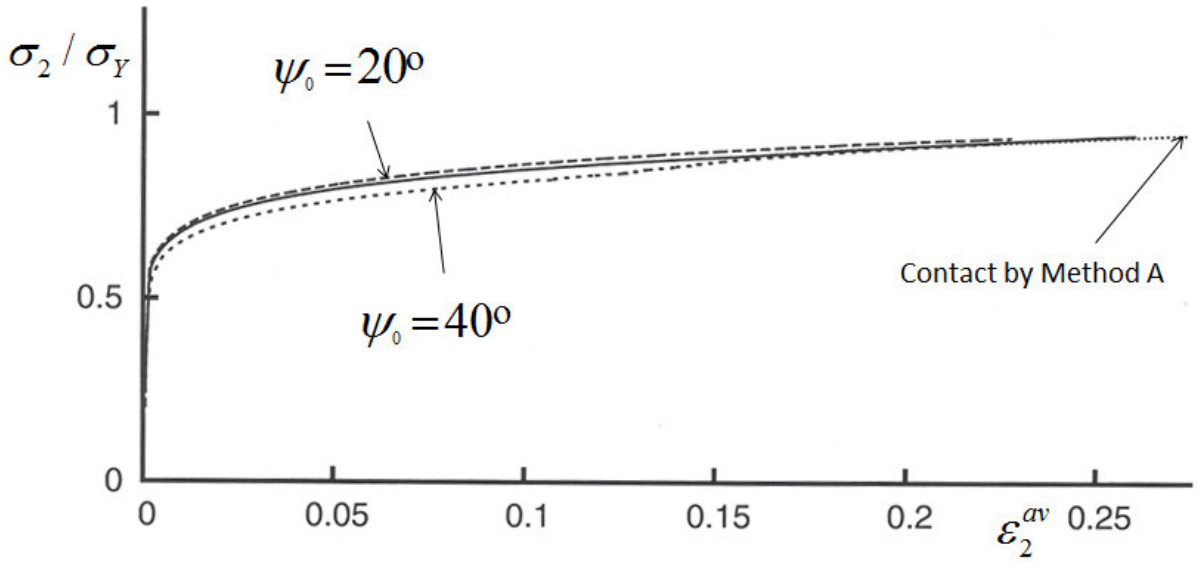

Fig. 7a. Curves of the true tensile stress σ_2 in the far field vs. the average logarithmic strain ε_2^{av}, for $B_0 / A_0 = 2$, $R_0 / D_0 = 0.175$ and $\kappa = -1.0$. Curves are shown for $\psi_0 = 20^o$ and for $\psi_0 = 40^o$, while the other two curves have $\psi_0 = 30^o$. One curve is based on contact method A, while the other three curves are based on method B.

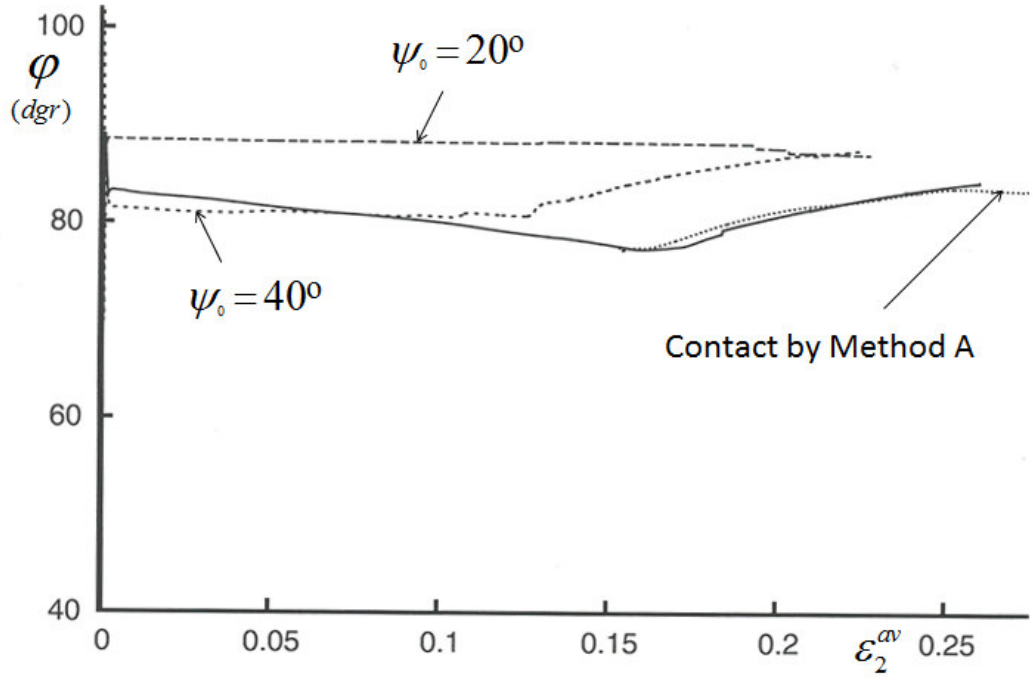

Fig. 7b. Curves of the angle φ between the x^1-axis and the axis of the elongated void vs. the average logarithmic strain ε_2^{av}, for $B_0 / A_0 = 2$, $R_0 / D_0 = 0.175$ and $\kappa = -1.0$. Curves are shown for $\psi_0 = 20^o$ and for $\psi_0 = 40^o$, while the other two curves have $\psi_0 = 30^o$. One curve is based on contact method A, while the other three curves are based on method B.

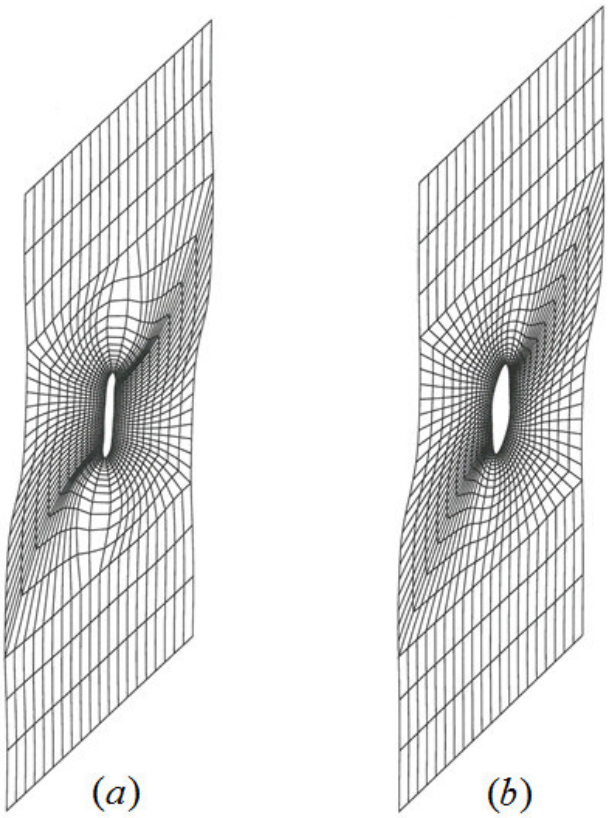

Fig. 8. Deformed meshes at the end of two different computations with $\kappa = -1.0$, $B_0 / A_0 = 2$ and $R_0 / D_0 = 0.175$. (a) Contact method B, at $\varepsilon_2^{av} = 0.261$. (b) Contact method A, at $\varepsilon_2^{av} = 0.275$.

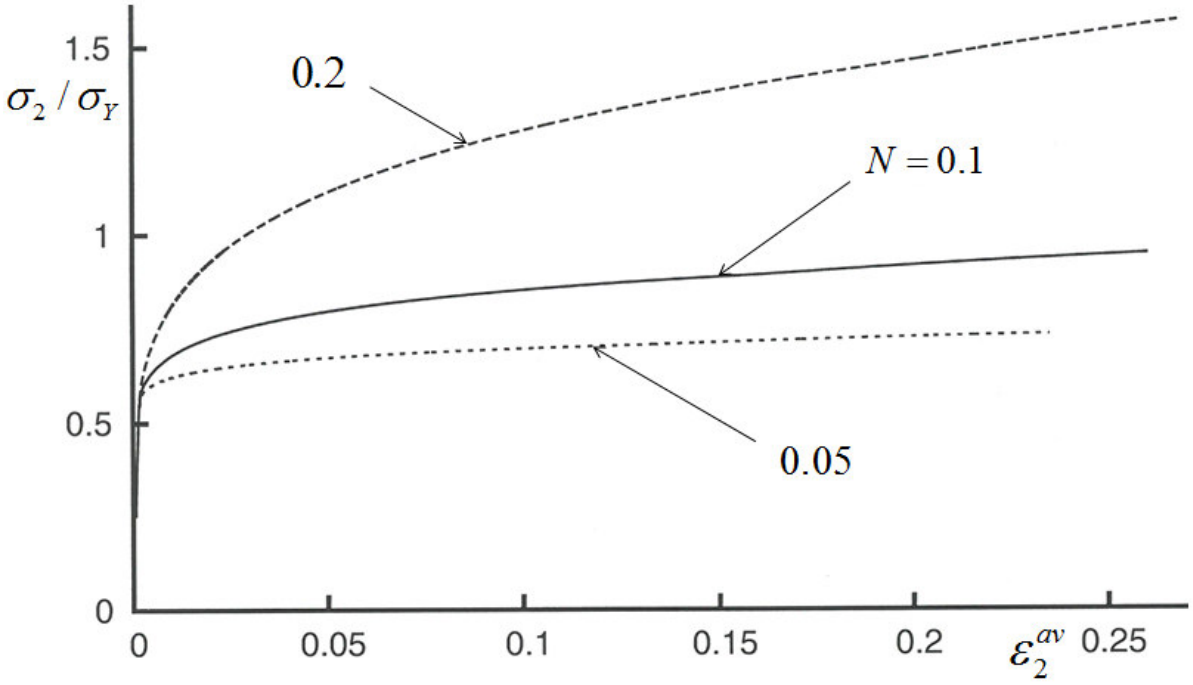

Fig. 9a. Curves of the true tensile stress σ_2 in the far field vs. the average logarithmic strain ε_2^{av}, for $B_0 / A_0 = 2$, $R_0 / D_0 = 0.175$, $\kappa = -1.0$ and various values of the hardening exponent N.

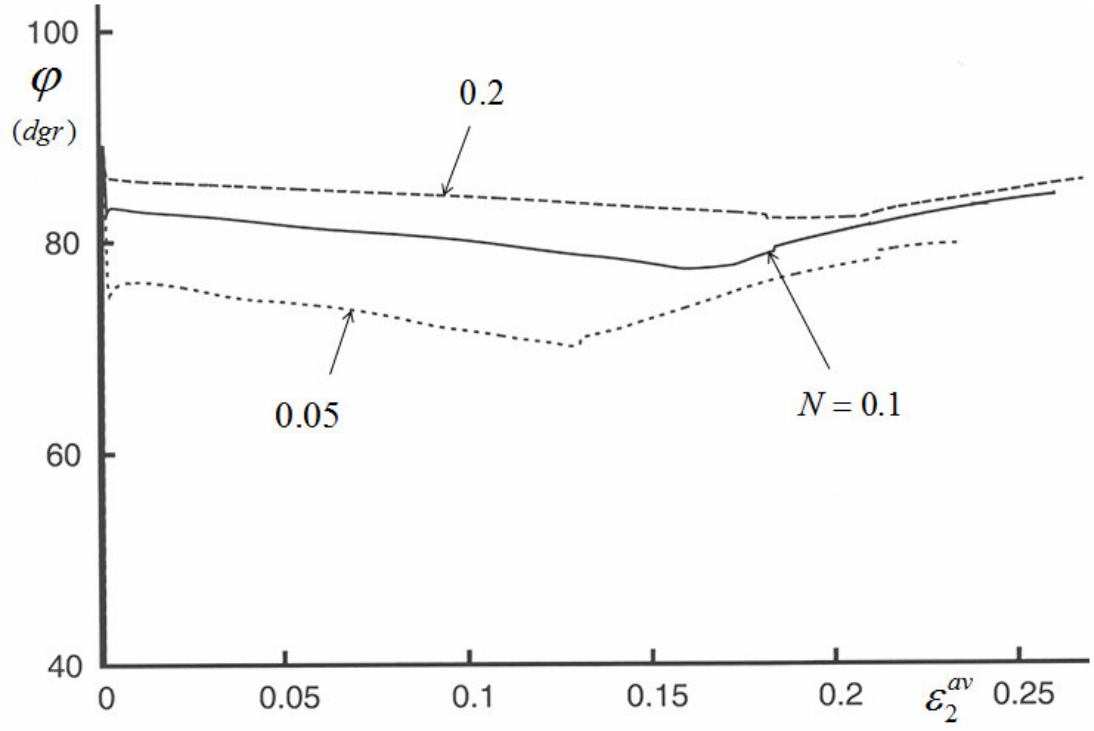

Fig. 9b. Curves of the angle φ between the x^1-axis and the axis of the elongated void vs. the average logarithmic strain ε_2^{av}, for $B_0 / A_0 = 2$, $R_0 / D_0 = 0.175$, $\kappa = -1.0$ and various values of the hardening exponent N.

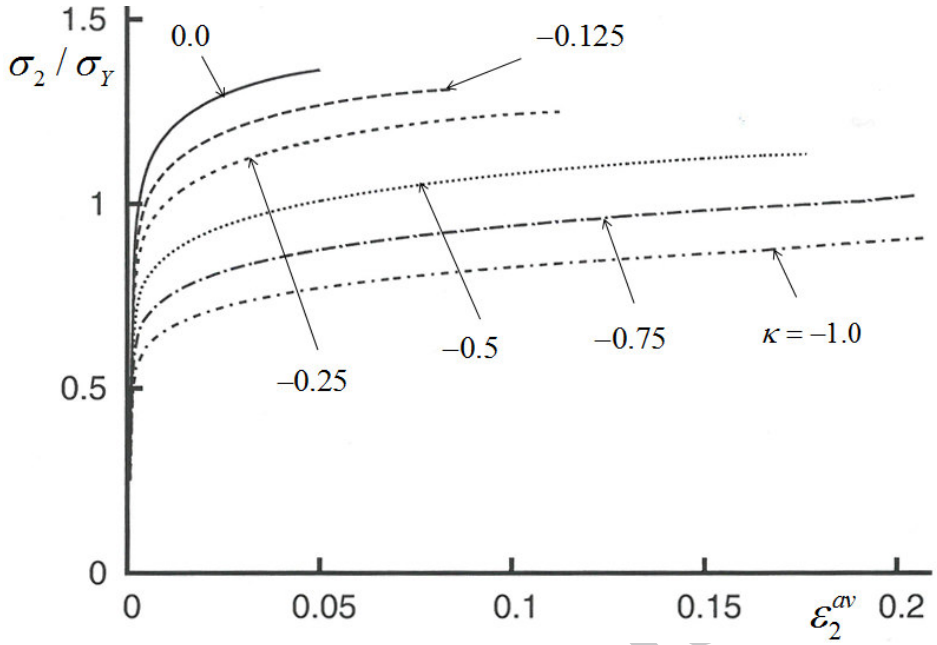

Fig. 10a. Curves of the true tensile stress σ_2 in the far field vs. the average logarithmic strain ε_2^{av}, for $B_0 / A_0 = 2$, $R_0 / D_0 = 0.25$ and various values of $\sigma_1 / \sigma_2 = \kappa$.

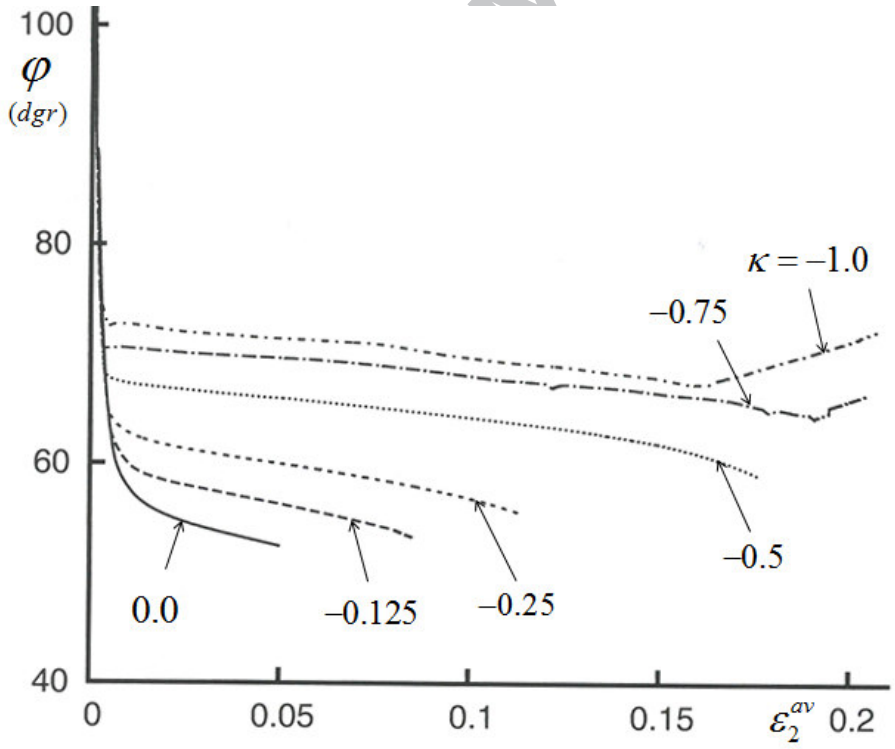

Fig. 10b. Curves of the angle φ between the x^1-axis and the axis of the elongated void vs. the average logarithmic strain ε_2^{av}, for $B_0 / A_0 = 2$, $R_0 / D_0 = 0.25$ and various values of $\sigma_1 / \sigma_2 = \kappa$.

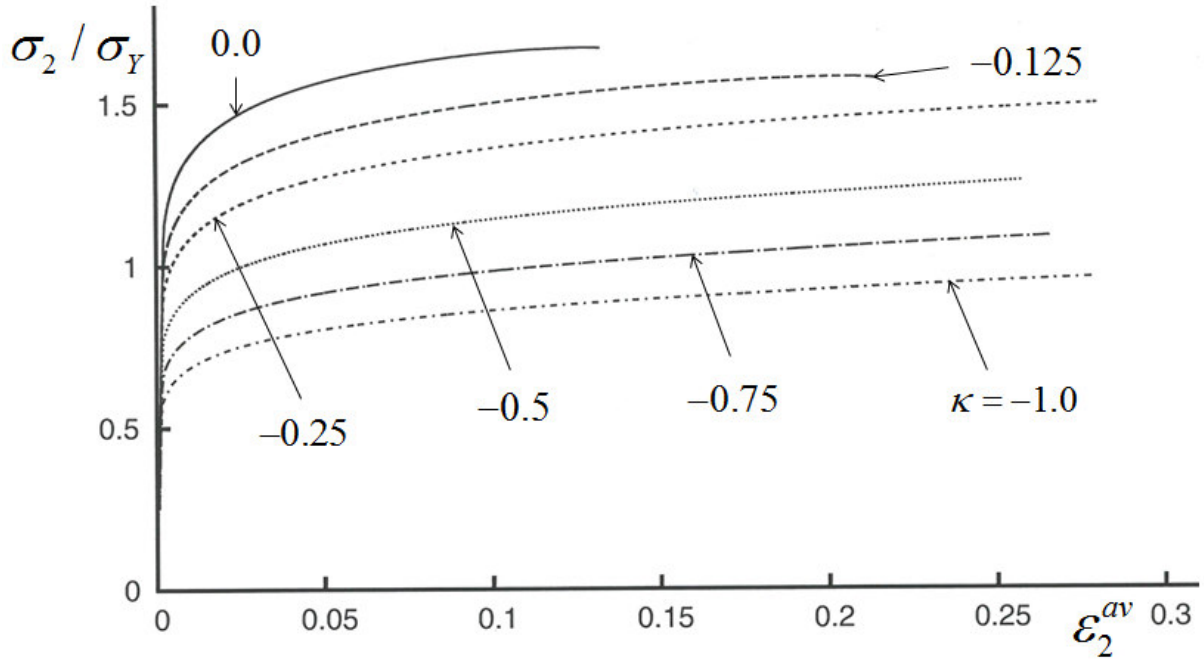

Fig. 11a. Curves of the true tensile stress σ_2 in the far field vs. the average logarithmic strain ε_2^{av}, for $B_0 / A_0 = 2$, $R_0 / D_0 = 0.125$ and various values of $\sigma_1 / \sigma_2 = \kappa$.

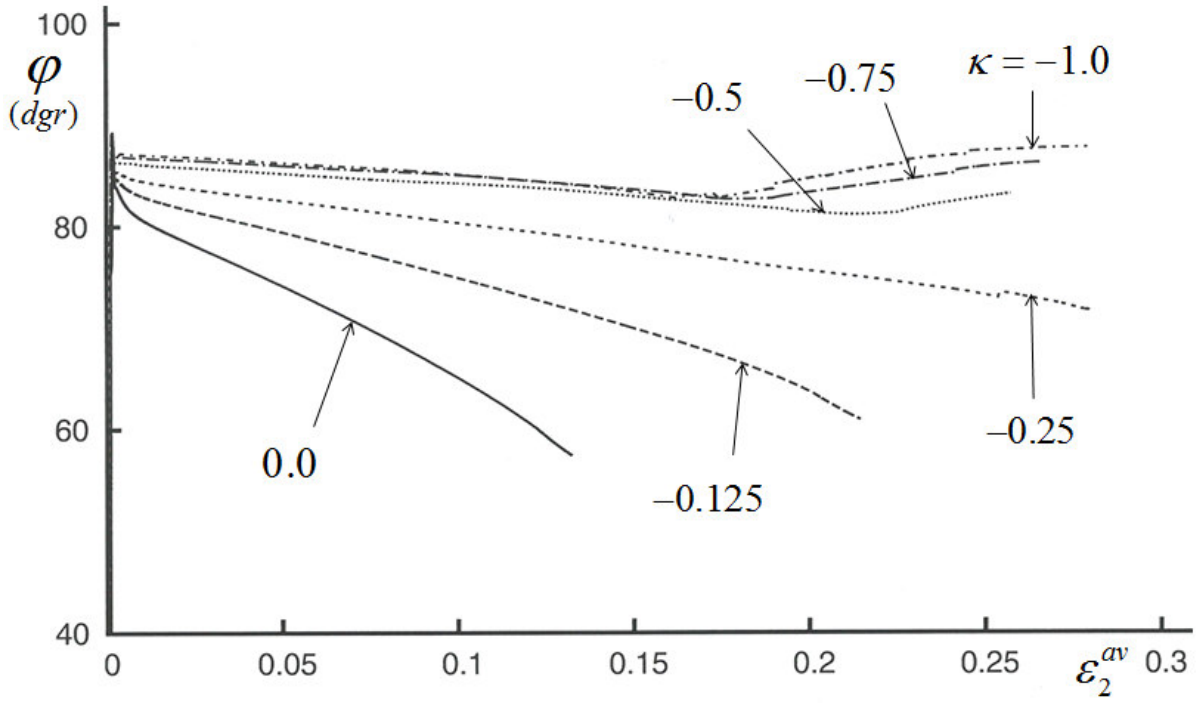

Fig. 11b. Curves of the angle φ between the x^1-axis and the axis of the elongated void vs. the average logarithmic strain ε_2^{av}, for $B_0 / A_0 = 2$, $R_0 / D_0 = 0.125$ and various values of $\sigma_1 / \sigma_2 = \kappa$.

- Imperfection in the form of an inclined sheet of voids.
- Ductile material subject to stress states in the vicinity of pure shear.
- Voids close up to form micro-cracks, which remain closed.
- Different initial void sizes and hardening are considered.
- No void sheet localization found for the low stress triaxialities.